RSC Advances

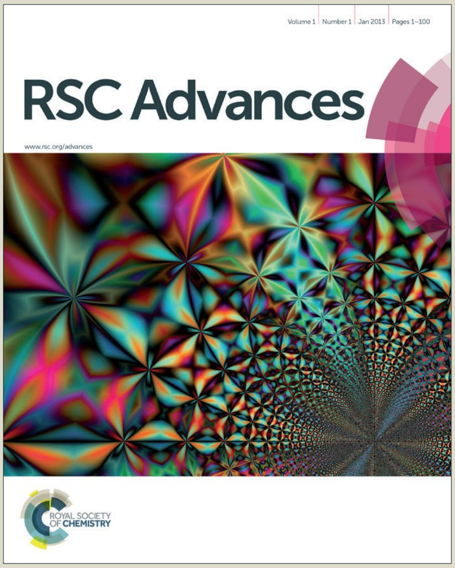

ROYAL SOCIETY OF CHEMISTRY

www.rsc.org/advances

Enhanced photocatalytic activity of magnetically separable bactericidal $CuFe_2O_4$-embeded Ag-deposited ZnO nanosheets

Chockalingam Karunakaran,* Pazhamalai Vinayagamoorthy, and Jayaraman Jayabharathi

Department of Chemistry, Annamalai University, Annamalainagar 608002, Tamilnadu, India

Corresponding author:

Professor Dr. C. Karunakaran
CSIR Emeritus Scientist
Department of Chemistry
Annamalai University
Annamalainagar 608002
Tamilnadu
India
E-mail: karunakaranc@rediffmail.com
Tel: +919443481590

Abstract

Mineralization of organic pollutants by semiconductor-photocatalysis is an emerging technique but recovery of the photocatalyst nanoparticles is the hindrance for putting this technology into practice. Magnetic separation is feasible if a magnetic core is implanted in the photocatalyst particle. Iron oxide core, because of the conduction and valence band potentials, promotes electron-hole recombination in the core/shell photocatalyst and thus suppresses the photocatalytic activity. Here we present for the first time, synthesis of magnetically recoverable bactericidal $CuFe_2O_4$-encapsulated Ag-deposited ZnO nanosheets for enhanced photocatalytic mineralization of dye; the CB edge of $CuFe_2O_4$ core does not induce charge carrier recombination. The nanosheets were obtained by a two-step synthesis of hydrothermal method followed by photodeposition. High resolution scanning and transmission electron microscopies, selected area electron and X-ray diffractometries, vibrating sample magnetometry, and energy dispersive X-ray, Raman, solid state electrochemical impedance, UV visible diffuse reflectance, photoluminescence and time-correlated single photon counting lifetime spectroscopies show encapsulation of $CuFe_2O_4$ in Ag-deposited ZnO nanosheets. The synthesized composite nanosheets show enhanced photocatalytic activity. The synthesized nanosheets are trifunctional material. The photocatalyst is photostable, reusable and magnetically separable. Furthermore, they exhibit excellent bactericidal activity.

Introduction

Emerging economies of some developing countries and increasing population, under globalization of economies, provide momentum for rapid industrial growth in some developing countries leading to large pollution of surface water. Photocatalytic mineralization of organic pollutants is an emerging technology. Band gap illumination of semiconductor nanocrystals generates electron-hole pairs, electron in the conduction band (CB) and hole in the valence band (VB).[1] While some of the photoformed charge carriers diffuse to the crystal surface, react with the species adsorbed and bring in photocatalysis the rest recombine suppressing the photocatalytic activity. Bacterial contamination of surface water is widespread in tropical regions. Use of inorganic bactericides in place of organics is of interest as they are stable and safe to handle. Nanocrystalline ZnO is one of the most attractive functional materials of industrial importance because of its direct band gap with large excitonic binding energy at room temperature, unique electronic properties and photocatalytic[2] and bactericidal[3] activities. The problem of separation of the photocatalytic nanocrystals is the hurdle in adopting this technology. Magnetic recovery is possible provided magnetic core is implanted in the photocatalytic nanoparticle.[4] In the implanted nanoparticle, the magnetic core is covered by the ZnO shell and is not exposed to the reactants like pollutants, air and moisture. Furthermore, the ZnO shell shields the core from the exciting radiation. That is, the core is protected by the shell from the reactants and also the radiation. The ZnO shell is photoexcited on illumination and is responsible for the photocatalytic activity. Core/shell Fe_3O_4/ZnO and Fe_2O_3/ZnO are of type-I core/shell band alignment and the cores are to induce charge carrier recombination.[5,6] The CB electron of ZnO shell is more cathodic than those of Fe_3O_4 and Fe_2O_3 and the VB hole of ZnO is more anodic than those of the iron oxides. Hence, migration of the photogenerated electron and hole from the ZnO shell to the iron oxide core resulting in their recombination is energetically favorable. This is to suppress the photocatalytic activity. Recently, Sing *et al*., synthesized Fe_3O_4 embedded ZnO nanocomposite for photocatalytic environmental remediation and observed that its photocatalytic activity is less than that of pristine ZnO.[7] Although there are a couple of reports of enhanced photocatalytic activity of Fe_2O_3/ZnO core/shell nanospindles the comparison was with the core Fe_2O_3 and not with ZnO which constitutes the shell.[8,9] $CuFe_2O_4$ is a magnetic oxide and its CB electron is more cathodic than that of ZnO.[10,11] Hence, promotion of recombination of charge carrier produced in ZnO shell by $CuFe_2O_4$ core is thermodynamically unviable and hence suppression of the photocatalytic activity is unlikely. Silver is well known for its antibacterial activity.[12-15] Furthermore, in Ag-deposited ZnO, silver is reported to trap the CB electron and transfer the same to the adsorbed oxygen molecule thereby enhance the photocatalytic activity;[16, 17] in semiconductor photocatalysis, reduction of oxygen molecule to superoxide radical ion ($O_2^{\bullet-}$) is slow.[18] Hence, to enhance the bactericidal and photocatalytic activities, the $CuFe_2O_4$-implanted ZnO nanosheets have been deposited with Ag. The synthesized Ag-deposited $CuFe_2O_4$-embedded ZnO nanosheets are trifunctional material, which are magnetically separable photocatalyst cum bactericide.

Experimental section

Synthesis

To $CuFe_2O_4$ nanocrystals (Sigma Aldrich, 0.025 g) dispersed in 10 mL of deionized distilled water by sonication an aqueous solution of polyethylene glycol 20000, PEG 20k (Himedia, 2 g in 10 mL) was added with stirring (15 min). To this was added drop by drop 0.5 M zinc acetate (10 mL) with stirring (30 min). To the resultant 0.5 g of polyvinyl pyrrolidone, PVP (Himedia) was added under stirring (15 min). This was followed by drop wise addition of 10 mL of 1 M urea, also with stirring. This was transferred into a 100 mL Teflon-lined autoclave vessel and heated in a hot air oven at 180 °C for 12 h. The content was allowed to cool of its own to room temperature, filtered, washed with distilled water and then ethanol several times, dried for 6 h at 120 °C and calcined for 2 h at 500 °C in a muffle furnace. The furnace was fitted with a PID temperature controller and the heating rate was set at 10 °C min^{-1}. Pristine ZnO was obtained by adopting the same procedure but without the addition of $CuFe_2O_4$ nanocrystals. The silver-deposited nanocomposite was prepared by photodeposition. The synthesized composite (0.3 g) was suspended in 25 mL of doubly distilled water containing 5 mg of $AgNO_3$ and 2 mL of methanol and air was bubbled through the solution continuously. The solution was irradiated for 8 h at 365 nm with eight 8 W mercury lamps. The completion of Ag deposition was tested by analytical method. The solid was collected by centrifugation, washed many times with water and ethanol and dried for 4 h at 120 °C.

Characterization

The high resolution scanning electron microscopic (HRSEM) images, the energy dispersive X-ray spectra (EDS) and the elemental mapping were obtained with a FEI Quanta FEG 200 HRSEM equipped with electron back scattered detection (BSD) and advanced technological PBS (WDS) in high vacuum mode. The sample was finely spread on carbon substrate. A JEOL JEM 2100 high resolution transmission electron microscope (HRTEM) was used to get the HRTEM images and the selected area electron diffraction (SAED) patterns. The sample was dispersed in ethanol and spread on the grid for imaging. Formavar coated copper grid was used for loading the sample. The SAED pattern was also obtained at an acceleration voltage of 200 kV with a Philips CM200 TEM attached with CCD camera. A PANalytical X'pert PRO diffractometer was used to record the X-ray diffraction (XRD) patterns in the 2θ range of 20 - 80° employing Cu Kα rays at 1.5406 Å with a tube current of 30 mA at 40 kV. The Raman spectrum was recorded with a Renishaw inVia Raman microscope. The sample was excited at 488 nm employing an argon laser as excitation source. A Lakeshore 7404 vibrating sample magnetometer was used to carry out magnetic measurements at room temperature. The UV-visible diffuse reflectance spectra (DRS) were obtained with a Shimadzu UV-2600 spectrometer with ISR-2600 integrating sphere attachment. A PerkinElmer LS 55 fluorescence spectrometer was employed to obtain the photoluminescence (PL) spectra at room temperature. The nanomaterials were dispersed in carbon tetrachloride under sonication and excited at 340 nm. A Horiba Jobin Yuon Fluorolog FL-3-11spectrofluorimeter was employed for the time-resolved fluorescence measurement. The nanosheets were excited with pulsed Nano-LED at 295 nm. The solid state electrochemical impedance spectra (EIS) were recorded at room temperature with a CH Instrument Electrochemical Analyzer 604C in the frequency range 0.1 MHz – 1 Hz. The disk area was 0.5024 cm^2 and the thickness of the pellets of Ag-deposited $CuFe_2O_4$ embedded ZnO, pristine ZnO and the precursor $CuFe_2O_4$ were 1.12, 1.87 and 1.42 mm, respectively.

Photodegradation

A photoreactor fixed with four 8 W medium pressure mercury vapor lamps (Sankyo Denki, Japan) illuminating predominantly at 365 nm was used to assess the photocatalytic degradation of dye. The light intensity was preserved in the photoreactor by the mounted highly polished anodized aluminum reflector. A borosilicate glass tube of 15 mm diameter was used as the reaction vessel. It was seated at the centre of the photoreactor. The heat generated was dissipated by the fans fixed at the bottom of the reactor. The light intensity was determined by ferrioxalate actinometry (25.4 μeinstein L^{-1} s^{-1}). Fresh solution of methylene blue (MB) was employed for the dye degradation study. Twenty five mg of the nanomaterial was added to 25 mL of the dye solution and air was bubbled through the solution to suspend the nanomaterial and keep it at continuous motion. After 15 min (to allow the adsorption process to attain equilibrium), it was illuminated. At varied illumination time, the magnetic composite and $CuFe_2O_4$ nanoparticles were recovered using a magnet and pristine ZnO was separated with membrane filter and the dye was estimated spectrophotometrically at 662 nm. A calibration curve was obtained by determining the absorption of MB at different ppm.

E. coli-inactivation

A nutrient broth of pH 7.4 was prepared by dissolving nutrient broth (13 g) in distilled water (1 L) and sterilized at 121 °C in an autoclave. MacConkey agar (55 g) dissolved in boiling distilled water (1 L) was sterilized at 121 °C in an autoclave and poured into Petri dish to get MacConkey agar plate. *Escherichia coli* (*E. coli*) bacteria were incubated in nutrient broth solution under shaking at 37 °C for 24 h. The cultured bacteria were centrifuged at 3500 rpm and washed with autoclaved 0.9% NaCl solution. The collected *E. coli* were suspended in 0.9% NaCl solution. The colony forming unit (CFU) was counted by a viable count method. Ten μL of the *E. coli* culture was streaked on the MacConkey agar plate and incubated at 37 °C for 24 h. Twenty mg of the composite nanosheets was added to 25 mL of the *E. coli* solution in a 60 mL bottle and shaken well continuously without any illumination. At the required time, the magnetic composite was removed from the solution and *E. coli* population was enumerated by a viable count method.

Result and discussion

Ag-deposited ZnO nanoflakes with $CuFe_2O_4$ core

Ag-deposited ZnO with $CuFe_2O_4$ core was obtained by a two-step synthesis of hydrothermal method followed by photodeposition of silver. The HRSEM images of the synthesized material are presented in Fig. 1. They show the prepared composite as nanosheets with length and breadth in thousands of nm (Fig. 1 a). The micrographs further show that the nanosheets are made up of nanoparticles. The nanocrystals are bound together two-dimensionally to form perforated nanosheets (Fig. 1b). Composite iron oxide is reported to have a high mass-thickness contrast[9] and in the HRTEM image of the nanosheets the embedded $CuFe_2O_4$ appears black (Fig. 1 c). The ZnO is of light color in the image. Further, the high magnification HRTEM image displays the core/shell structure of the synthesized composite nanosheets; the black $CuFe_2O_4$ core and the grey hexagonal ZnO shell are seen. The EDS of Ag-deposited $CuFe_2O_4$-embedded ZnO is displayed in Fig. 2 (a). It shows the presence of all the constituent elements. The absence of any other element reveals the purity of the synthesized sample. The EDS analysis provides the composition of deposited Ag as 0.4 at. %. Fig. 2 also presents the elemental mapping of the synthesized composite. It shows uniform and dense distribution of zinc and oxygen throughout the specimen (Fig. 2 b and d). The distribution of silver is also uniform but sparse (Fig. 2 c). This shows uniform deposition of silver and is in agreement with its low percentage of deposition. The SAED patterns of the synthesized nanosheets, recorded at different areas with two different instruments, are displayed in Fig. 3. They show the reflection spots of 100, 101, 102, 110, 103, 112, 201 and 203-planes of hexagonal ZnO. JCPDS card no. 36-1451is the reference employed. Furthermore, the SAEDs display the diffraction patterns of cubic and tetragonal $CuFe_2O_4$. The diffraction spots index to 511, 440 and 731-planes of cubic $CuFe_2O_4$ and 220, 204, 321 and 400-planes of tetragonal $CuFe_2O_4$. The references adopted for the cubic and tetragonal $CuFe_2O_4$ are JCPDS cards 25-0283 and 34-0425, respectively. The SAEDs also show the diffraction spots of

200 and 220-planes of face centered cubic Ag; the standard used is JCPDS card no. 04-0783. Thus, the EDS, elemental maps and SAEDs show the synthesized nanosheets as Ag-deposited $CuFe_2O_4$ embedded ZnO.

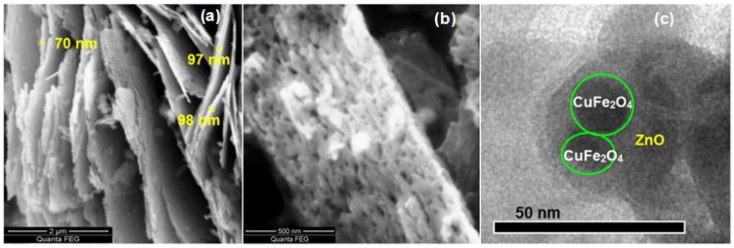

Fig. 1 HRSEM images (a and b) and HRTEM image displaying the core (c) of $CuFe_2O_4$-implanted Ag-deposited ZnO nanosheets.

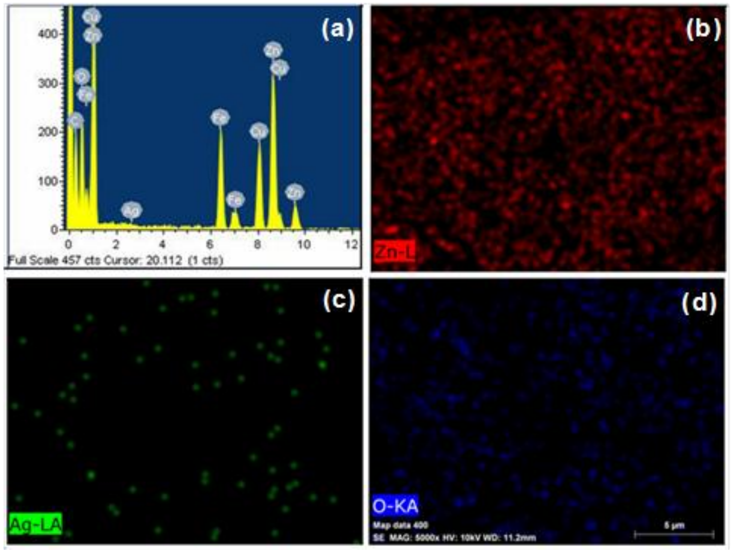

Fig. 2 EDS (a) and elemental mapping (b, c, and d) of the synthesized nanosheets.

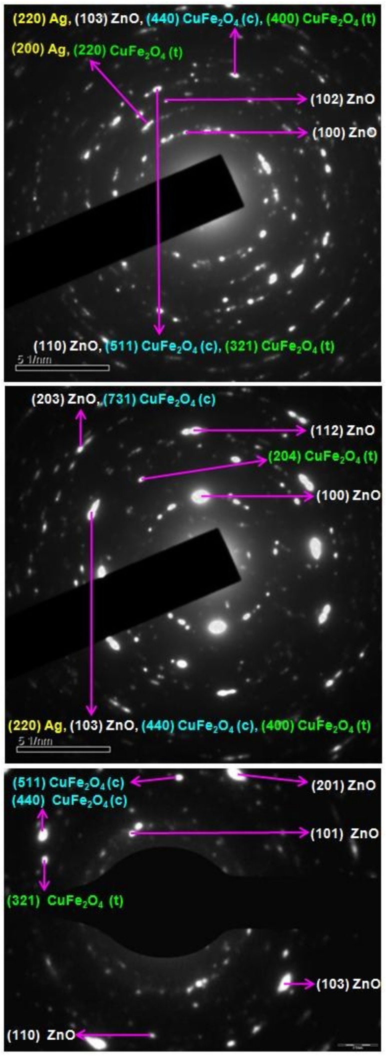

Fig. 3 SAEDs of Ag-deposited CuFe$_2$O$_4$-embedded ZnO nanosheets.

The XRD of CuFe$_2$O$_4$ embedded Ag-deposited ZnO nanosheets is presented in Fig. 4. The diffractogram is in agreement with that of hexagonal ZnO. JCPDS card no. 36-1451 is the reference used. Further, the 111-peak of face centered cubic lattice of metallic Ag is observed (JCPDS 04-0783). But none of the XRD peaks of either cubic or tetragonal CuFe$_2$O$_4$ has been observed in the recorded diffractogram. These XRD results confirm that CuFe$_2$O$_4$ is perfectly encapsulated in the Ag-deposited ZnO nanosheets. It has been reported that increase of the quantity of zinc precursor employed for the synthesis decreases the intensity of the XRD peaks of the core and increases the intensity of reflection by ZnO.[19,20] A perfect thick coating of ZnO completely suppresses the X-ray diffraction by the core.[21] With the increase of the order of diffraction (n) the intensity of XRD peak is to decrease rapidly and the order of diffraction by the crystal plane of the core is to correspond to the thickness of the shell. The XRD of pristine ZnO nanoflakes is also displayed in Fig. 4 for comparison. As in the composite nanosheets ZnO in pristine ZnO exists in wurtzite structure. Fig. 4, in addition, presents the XRD pattern of precursor $CuFe_2O_4$. It shows the precursor as a blend of tetragonal and cubic phases; JCPDS card nos. 34-0425 and 25-0283 are the references employed for tetragonal and cubic $CuFe_2O_4$, respectively. The observed 400 and 440-peaks at 43.1 and 62.7°, respectively, are characteristic of cubic $CuFe_2O_4$ lattice. The peak at 53.8° corresponds to the 312-plane of tetragonal $CuFe_2O_4$. The molar fraction (X_i) of tetragonal and cubic phases of $CuFe_2O_4$ in the precursor has been obtained as 0.19 and 0.81, respectively. The formula employed is $X_i = S_i/\Sigma S_i$, where S_i is the peak area of the most intense reflections of each phase.[22]

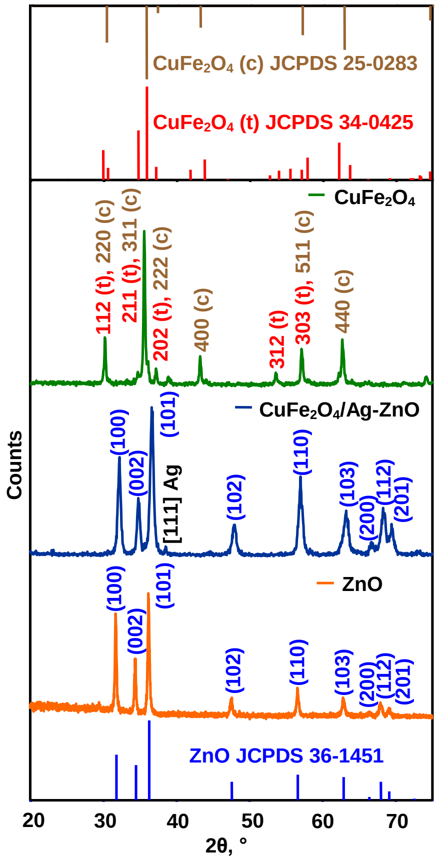

Fig. 4 XRDs of Ag-deposited $CuFe_2O_4$-implanted ZnO and pristine ZnO nanosheets and precursor $CuFe_2O_4$ nanoparticles.

The Raman spectrum of the synthesized composite supports the perfect encapsulation of $CuFe_2O_4$ by ZnO. ZnO is of hexagonal wurtzite crystal structure and belongs to $P6_3mc$ space group.[23,24] Each zinc ion is tetrahedrally surrounded by four oxide ions and vice versa. The irreducible representations are A_1, $2B_1$, E_1 and $2E_2$ out of which A_1, E_1 and E_2 are Raman active. Furthermore, A_1 and E_1 are polar and split into longitudinal (LO) and transverse (TO) optical modes. The E_2 symmetry has two frequencies, E_2(high) and E_2(low). Fig. 5 displays the Raman spectrum of $CuFe_2O_4$ embedded Ag-deposited ZnO nanosheets. The peak at 96 cm^{-1} corresponds to E_2(low) of wurtzite lattice.[23-30] The E_2(low) mode is associated with the vibration of the zinc sublattice.[29] The absence of E_2(high) mode may likely be because of implantation of $CuFe_2O_4$ in ZnO lattice and also deposition of Ag. This may also be a reason for the suppression of A_1(TO) mode. The peak at 561 cm^{-1} is attributed to the E_1(LO) mode.[24] Generally, the E_2(high) mode is ascribed to the lattice vibration of ZnO and the E_1(LO) mode is associated with defects in ZnO such as oxygen vacancy or other defect states.[24] The peak at 318 cm^{-1} can be assigned to the second-order Raman spectrum arising out of E_2(high)-E_2(low).[28] A broad hump at around 660 cm^{-1}is likely due to the surface phonon scattering from zone-boundary phonons, $2E_2(M) + A_1(LO)$.[25,27] The broad peak at 1149 cm^{-1} is attributed to the second-order (2LO) Raman mode.[25] Thus, the XRD and Raman spectrum confirm perfect encapsulation of $CuFe_2O_4$ by ZnO lattice in the synthesized nanoflakes.

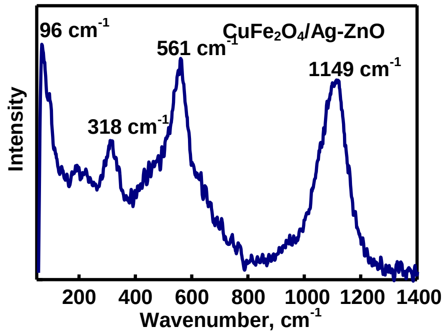

Fig. 5 Raman spectrum of Ag-deposited $CuFe_2O_4$ embedded ZnO nanosheets.

Magnetic core

The magnetization (M) of the composite nanosheets as a function of applied field (H), recorded at room temperature, is shown in Fig. 6 a. The saturation magnetization (M_S), coercivity (H_C) and remanence magnetization (M_R) have been obtained from the M-H curve. The size and shape of the hysteresis curve are characteristic of the material and the obtained hysteresis loop is of normal S-shape. The loop indicates a significant content of ferrimagnetic material in the composite nanosheets The ‘thickness’ of the middle of the *S*-shaped loop shows the amount of hysteresis, which represents the coercivity of the material. The coercivity of the composite nanosheets is 0.54 kOe. This is comparable to the coercivities of $CuFe_2O_4$ nanoparticles obtained by (i) epoxide-assisted sol-gel method and calcined at 400 (0.43 kOe) and 600 °C (0.83 kOe),[25] (ii) sol-gel technique (0.64 kOe),[31] (iii) coprecipitation method (0.57 kOe)[32] and (iv) microwave-induced combustion synthesis (0.60 kOe).[33] Fig. 6 also displays the hysteresis loop of precursor $CuFe_2O_4$ nanoparticles. The normal *S*-shaped loop shows the precursor as superparamagnetic. Its coercivity is insignificant (0.08 kOe) and is comparable to that of $CuFe_2O_4$ nanoparticles prepared by epoxide-assisted route and calcined at 500 °C (0.07 kOe).[22] The M_R of the composite nanosheets (0.60 emu g^{-1}) is larger than that of precursor $CuFe_2O_4$ (0.07 emu g^{-1}) but is smaller than those of $CuFe_2O_4$ nanoparticles obtained by coprecipitation method (10.7 emu g^{-1})[32] and epoxide-assisted sol-gel technique and calcined at 400, 500 and 600 °C (4.81, 0.99 and 9.54 emu g^{-1}, respectively.[22] The saturation magnetization of the composite nanosheets (1.74 emu g^{-1}) is larger than that of precursor $CuFe_2O_4$ nanoparticles (0.87 emu g^{-1}) and hence the efficiency of magnetic separation of the composite nanosheets may not be less than that of precursor $CuFe_2O_4$ nanoparticles. The M_S of precursor $CuFe_2O_4$ is very much less than those of nanoparticulate $CuFe_2O_4$ prepared by modified sol-gel technique (33.4 emu g^{-1}),[31] combustion method (30 emu g^{-1}),[34] microwave-induced combustion synthesis (21.2 emu g^{-1}),[33] surfactant free polyol method (8.35 emu g^{-1}),[35] epoxy-assisted route (17.1 emu g^{-1}),[22] hydrothermal method (83.7 emu g^{-1}),[36] coprecipitation method (35.6 emu g^{-1})[37] and ceramic process (42.5 emu g^{-1}).[38] A possible reason is that the precursor is a blend of 19% tetragonal and 81% cubic $CuFe_2O_4$. The *M-H* curve of hydrothermally synthesized pristine ZnO confirms the non-magnetic nature of the ZnO shell. The synthesized composite nanosheets are magnetically separable (Fig. 6 b).

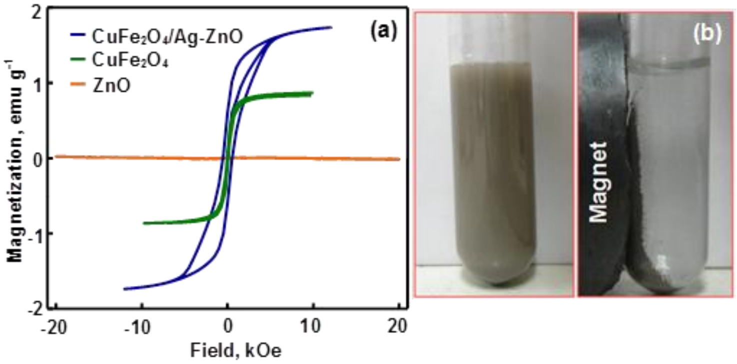

Fig. 6 *M-H* curves (a) and magnetic separation (b) of Ag-deposited $CuFe_2O_4$-embedded ZnO nanosheets.

Charge transfer resistance

The dynamics of charges in the bulk or interfacial region of semiconductor could be studied by solid state impedance spectroscopy. In polycrystalline materials, the overall crystal resistance is a combination of intragranular or bulk resistance and intergranular or grain boundary resistance. The Nyquist plot is a standard format of evaluating the impedance data. Fig. 7 presents the complex solid state impedance spectra of the synthesized composite nanosheets and pristine ZnO. The corresponding spectrum of precursor $CuFe_2O_4$ nanoparticles is also displayed for comparison. The grain boundary or intergranular resistance affords the ohmic or uncompensated resistance and the polarization or charge transfer resistance corresponds to the intragranular or bulk crystal resistance. The charge transfer resistance is related to Warburg resistance, which is the resistance to mass transfer and is governed by the specific conductance. The Nyquist plots show that the charge transfer resistance of the Ag-deposited composite nanosheets is very much larger than that of pristine ZnO. The charge transfer resistance of precursor $CuFe_2O_4$ nanoparticles is very small than that of pristine ZnO. The observed large charge transfer resistance of Ag-deposited $CuFe_2O_4$-implanted ZnO nanosheets is likely due to its heterogeneity.

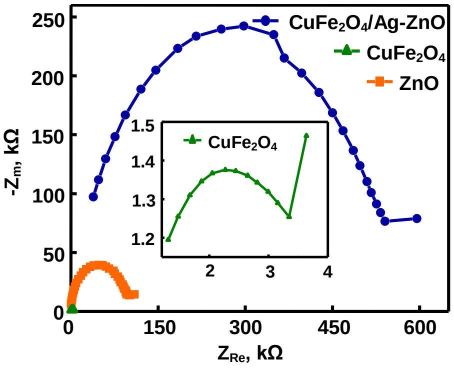

Fig. 7 Nyquist plots of Ag-deposited CuFe$_2$O$_4$-implanted ZnO and pristine ZnO nanosheets and precursor CuFe$_2$O$_4$ nanoparticles.

Band gap, emission and charge carrier radiative recombination

The DRS of the synthesized Ag-deposited magnetic composite nanosheets and pristine ZnO are shown in Fig. 8 a. The DRS of precursor CuFe$_2$O$_4$ nanoparticles is also presented for comparison. The DRS are displayed in terms of $F(R)$, obtained from the determined reflectance (R) by using the Kulbaka-Munk (K-M) function [$F(R) = (1 - R)^2/2R$]. The DRS of pristine ZnO shows photoexcitation by UV-A light; the absorption shoots up at ~386 nm. The synthesized Ag-deposited magnetic composite nanosheets exhibit strong absorption of UV-A light. Furthermore, significant visible light absorption is also observed. This may be because of the surface plasmon resonance of Ag nanodeposits. The presence of CuFe$_2$O$_4$ core in the nanosheets may also be a reason for the observed visible light absorption. The recorded DRS of precursor CuFe$_2$O$_4$ is in agreement with the reported band gap (1.4 eV).[10] The modified K-M plots of $[F(R)h\nu]^2$ versus photon energy provide the direct band gaps of the composite nanosheets and pristine ZnO as 3.16 and 3.25 eV, respectively (Fig. 8 b). This is in support of the ZnO shell of the synthesized magnetic composite nanosheets.

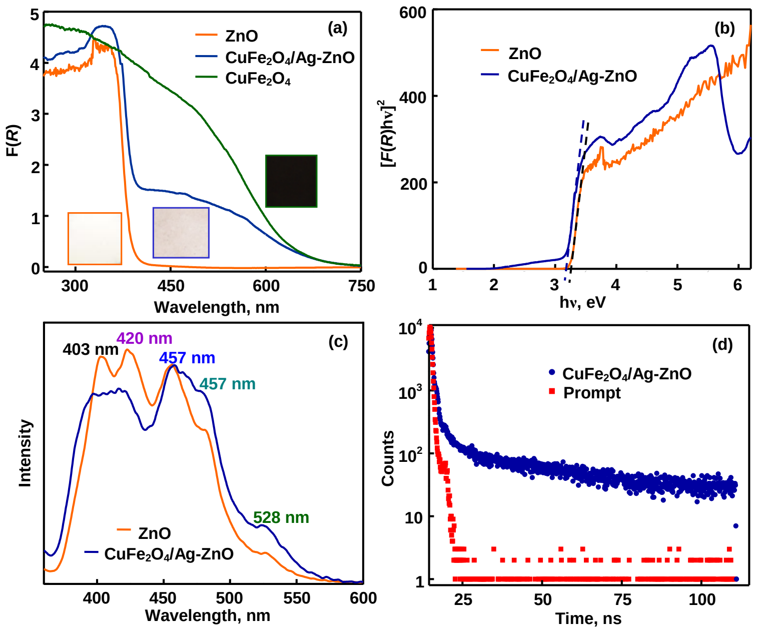

Fig. 8 DRS (a), Tauc plot (b) and PL (c) and TRPL (d) spectra of Ag-deposited $CuFe_2O_4$ embedded ZnO nanosheets.

The normalized PL spectra of the synthesized magnetic Ag-deposited nanosheets and pristine ZnO, recorded at room temperature, are presented in Fig. 8 (c). The PL spectra do not differ significantly and thus confirm perfect encapsulation of $CuFe_2O_4$ core by ZnO lattice. Both the nanomaterials exhibit near band gap (NBE) and deep level emissions (DLE). The DLE is due to different intrinsic and extrinsic structural defects in the ZnO shell of $CuFe_2O_4$-implanted Ag-deposited ZnO and pristine ZnO nanosheets.[24,39] The NBE originates from the recombination of photoformed electron-hole pairs. The violet emission at ~420 nm, blue emission at ~457 nm and blue-green emission at ~481 nm are attributed to the band-edge free excitons and bound excitons.[40,41] The blue emission originates from the electron transition from the shallow donor level of oxygen vacancies to the VB and electron transition from the shallow donor level of zinc interstitials to the VB.[41] The green emission exhibited at 528 nm is associated with oxygen vacancies and other vacancy related defects.[24] The energy of electron transition from deep-level donor of the ionized oxygen vacancies to the VB corresponds to this emission. Yellow emission stems from excess oxygen and absence of such emission suggests that there is no excess oxygen in the synthesized nanoflakes.[24] Semiconductor ZnO which constitutes the shell is of n-type and the core $CuFe_2O_4$ is a p-type semiconductor. This results in formation of p-n junction at the interface of the lattices of ZnO and $CuFe_2O_4$ in $CuFe_2O_4$ implanted ZnO deposited with Ag. Considering the CB energy of ZnO (-4.19 eV) and VB energy of $CuFe_2O_4$ (-4.71 eV) quenching of CB electron of ZnO by VB hole of $CuFe_2O_4$ is thermodynamically feasible if ZnO and $CuFe_2O_4$ are coexcited by UV light. However, such quenching is insignificant in the present case; the PL spectra do not show remarkable suppression of NBE of ZnO in Ag-deposited $CuFe_2O_4$ embedded ZnO nanosheets in comparison with pristine ZnO. A possible reason for the observed behavior is that the synthesized core/shell nanomaterial is not particles but sheets.

Time-resolved photoluminescence (TRPL) is a potent tool to probe the radiative charge carrier recombination in nanocrystalline semiconductors. The lifetime of excitons can be determined by time-correlated single photon counting (TCSPC) lifetime spectroscopy. The NBE of the synthesized $CuFe_2O_4$-implanted Ag-deposited ZnO nanosheets is at 393 nm and the TRPL traces were obtained at 395 nm; free exciton band corresponds to this wavelength of emission. Fig. 8 d shows the fluorescence decay. The excitation energy of 4.20 eV is very much larger than the band gap energy and the excitation first undergoes thermalization to form an exciton, which further relaxes before it radiates. Theses relaxation processes are very fast at room temperature.[42] The TRPL data fit satisfactorily to a single-exponential decay, $F(t) = a \exp(-t/\tau)$, where the pre-exponential term a is related to the concentration of the emitting species, τ is the measured time and $F(t)$ is the photon count at time t. The determined radiative lifetime of the charge carriers is 7 ps. The observed very short lifetime indicates the direct surface recombination of CB electron and VB hole.[43] The reported lifetimes of trapped charged carriers in ZnO are 1[42] and 1.5-2.8 ns[44] and that of shallowly trapped electron-deep trapped hole is 14-26 ns.[44] The measured PL decay time (τ_{PL}) is determined by radiative decay time (τ_R) as well as the non-radiative decay time (τ_{NR}) and hence τ_{PL} is shorter than τ_R. The τ_R and τ_{NR} are related by $(1/\tau_{PL}) = (1/\tau_R) + (1/\tau_{NR})$.[42] The τ_{NR} includes nonradiative processes like capture by deep traps and multiphoton emission. Thus the TCSPC lifetime spectroscopy shows that in the synthesized $CuFe_2O_4$-implanted Ag-deposited ZnO nanosheets surface recombination is predominant and recombination of trapped charge carrier in bulk is insignificant.

Enhanced photocatalytic activity

Fig. 9 a displays the UV visible spectra of the dye solution illuminated with the synthesized Ag-deposited $CuFe_2O_4$-implanted ZnO nanosheets. The time scan shows that the dye is effectively photodegraded by the synthesized composite nanosheets. The concentration-time profile of the degradation is also presented in Fig. 9 b. The dye-degradation was also tested under identical experimental conditions using pristine ZnO nanosheets and precursor $CuFe_2O_4$ nanoparticles. The concentration-time profiles displayed in Fig. 9 b show that the photocatalytic activity of Ag-deposited $CuFe_2O_4$ embedded ZnO nanosheets is larger than that of pristine ZnO nanosheets and precursor $CuFe_2O_4$ nanoparticles. Furthermore, reuse of the synthesized composite nanosheets for photocatalytic degradation shows that the photocatalytic activity is sustainable; Fig. 10 presents the dye degradation profiles up to 4-times of reuse. Moreover, the composite nanosheets are photostable. Estimation of zinc ion in the reaction solution before and after photodegradation of the dye by atomic absorption spectral analysis reveals absence of release of zinc ion due to the photocatalytic process under the experimental conditions. Although visible light-photocatalysis by $CuFe_2O_4$ is well known the UV light-photocatalytic activity of precursor $CuFe_2O_4$ nanoparticles is insignificant. A possible reason is the crystal structure of the precursor; it is a blend of cubic and tetragonal $CuFe_2O_4$. The photocatalytic efficiency of ZnO can be improved by depositing it with metallic silver.[16,17] The nanodeposits of Ag on the surface of ZnO may act as sink for the photogenerated electron and thus enhance transfer of CB electron of ZnO to acceptor molecules. The band gap of Ag-deposited composite nanosheets does not differ significantly from that of pristine ZnO nanosheets and hence is not a reason for the observed improved photocatalytic activity. The composite nanoflakes exhibit significant absorbance in the visible region which is because of the encapsulated $CuFe_2O_4$ core and to the surface plasmon resonance by Ag nanodeposits. The surface plasmon resonance of nano Ag, which can be excited by visible light, increases the electric field around metal particles, enhances surface electron excitation and thus electron-hole separation on Ag-deposited ZnO in presence of acceptor molecules. However, the visible light absorption is unlikely to be a reason for the observed enhancement of UV light-photocatalysis.

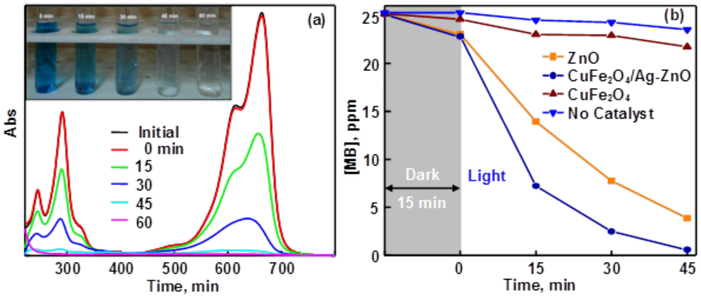

Fig. 9 Time scan-spectra (a) and decay profile (b) of dye-mineralization by Ag-deposited $CuFe_2O_4$-implanted ZnO nanosheets.

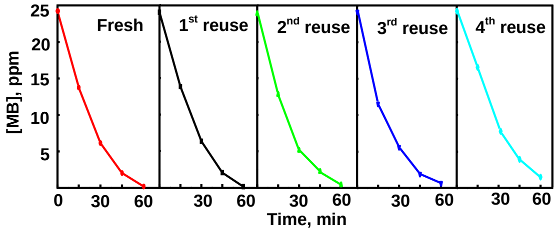

Fig. 10 Reusability of Ag-deposited $CuFe_2O_4$ embedded ZnO nanosheets as photocatalyst.

Silver nanodeposits on ZnO surface can act as electron sink.[16,17] The Fermi level of silver is lower than that of ZnO and the movement of photogenerated electrons from the CB of ZnO, leaving behind the holes in the VB, to the silver particles deposited on the surface of ZnO is thermodynamically feasible (Fig. 11). The difference between the Fermi levels leads to the formation of a Schottky barrier at the Ag/ZnO interface. This promotes electron migration from the CB of ZnO to Ag. The transferred electrons are trapped by metallic silver due to its strong electron-accepting ability. Accordingly, in presence of acceptors, more electrons and holes can be utilized. This leads to enhanced photocatalysis. In addition, the deposition of silver has a positive effect on the scavenging of the photogenerated electrons by O_2.[45] The slow step in photocatalytic oxidation is believed to be electron transfer from the semiconductor oxide surface to the adsorbed O_2, whereas in Ag-deposited $CuFe_2O_4$-implanted ZnO-photocatalysis the electron transfer is from the metallic silver to O_2; the detailed mechanism of Ag-deposited semiconductor-photocatalysis has been discussed elsewhere.[16,17,45] The VB of encapsulated $CuFe_2O_4$ core is less anodic than that of ZnO shell. Hence migration VB hole from ZnO shell to $CuFe_2O_4$ core is thermodynamically feasible. However, the CB electron of ZnO shell is less cathodic that of $CuFe_2O_4$ core and hence flow of photoformed electron from ZnO shell to $CuFe_2O_4$ core is energetically forbidden. Therefore, quenching of charge carriers formed on ZnO surface by $CuFe_2O_4$ core is unviable. That is, in the absence of consumption of holes in $CuFe_2O_4$

core (migrated from the ZnO shell) by substrates and the movement of photoformed electron from the ZnO shell to the $CuFe_2O_4$ core thermodynamically forbidden, the $CuFe_2O_4$ core cannot store holes and hence the $CuFe_2O_4$ core does not promote charge carrier recombination.

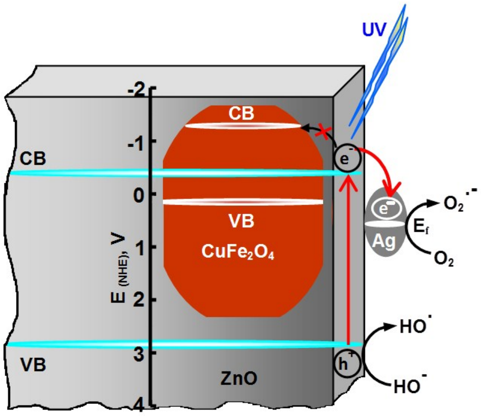

Fig. 11 Photocatalytic mechanism.

Bacteria inactivation

The synthesized Ag-deposited $CuFe_2O_4$ implanted ZnO nanosheets display bactericidal activity. Fig. 12 shows the inactivation of *E. coli* by the composite nanosheets in aqueous suspension without any illumination; *E. coli* of population 2.2 x 10^{11} CFU mL^{-1} has been completely inactivated in 10 min. In the absence of the nanoflakes the *E. coli* population remains unaffected. *E. coli* in 0.9% saline were employed for the evaluation of the antibacterial activity. The population of *E. coli* was determined by a viable count method on MacConkey agar plates after proper dilution of the culture. The bactericidal activity of Ag nanoparticles has been well established[12-15] and the antibacterial activity of ZnO is also known.[3] The mechanism of disinfection of bacteria by the synthesized Ag-deposited $CuFe_2O_4$ encapsulated ZnO nanosheets is likely to be similar to those reported.[3,12,46]

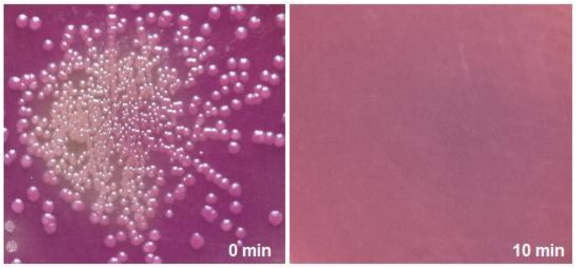

Fig. 12 Inactivation of *E. coli* by Ag-deposited $CuFe_2O_4$ embedded ZnO nanosheets.

Conclusions

Ag-deposited ZnO nanosheets with $CuFe_2O_4$ core have been obtained by a two-step synthesis of hydrothermal method followed by photoreduction of silver ion. The HRSEM, HRTEM, SAED, EDS, elemental mapping, XRD, VSM and Raman, UV visible DRS, PL and TRPL spectroscopies confirm perfect implantation of $CuFe_2O_4$ core in the Ag-deposited ZnO nanosheets. The CB of $CuFe_2O_4$ is more anodic than that of ZnO and the core does not promote electron-hole recombination. The synthesized composite nanosheets show enhanced photocatalytic activity. They are reusable, photostable and magnetically recoverable. Furthermore, they exhibit high bactericidal activity. Thus the synthesized Ag-deposited ZnO nanosheets with $CuFe_2O_4$ core are a trifunctional material, magnetically separable photocatalytic bactericide.

Acknowledgements

The financial support for the research (SR/S1/PC-41/2011) by the Science and Engineering Research Board (SERB), Department of Science and Technology (DST), New Delhi is gratefully acknowledged. Further, Prof. C. Karunakaran thanks the Council and Scientific and Industrial Research (CSIR), New Delhi, for the Emeritus Scientist Scheme 21(0887)/12/EMR-II. P. Vinayagamoorthy is grateful to DST for the fellowship.

References

1 J. Schneider, M. Matsuoka, M. Takeuchi, J. Zhang, Y. Horiuchi, M. Anpo and D. W. Bahnemann, Understanding TiO_2 photocatalysis: mechanisms and materials, *Chem. Rev.*, 2014, **114**, 9919-9986.

2 J. Wang, Z. Wang, B. Huang, Y. Ma, Y. Liu, X. Qin, X. Zhang and Y. Dai, Oxygen vacancy induced band-gap narrowing and enhanced visible light photocatalytic activity of ZnO, *ACS Appl. Mater. Interface*s, 2012, **4**, 4024-4030.

3 K. R. Raghupathi, R. T. Koodali and A. C. Manna, Size-dependent bacterial growth inhibition and mechanism of antibacterial activity of zinc oxide nanoparticles, *Langmuir*, 2011, **27**, 4020-4028.

4 S. Shylesh, V. Schunemann and W. R. Thiel, Magnetically separable nanocatalysts: bridges between homogeneous and heterogeneous catalysis, *Angew. Chem. Int. Ed*., 2010, **49**, 3428-3459.

5 A. M. Smith and S. Nie, Semiconductor nanocrystals: structure, properties, and band gap engineering, *Acc. Chem. Res*., 2010, **43**, 190-200.

6 P. Reiss, M. Protiere and L. Li, Core/shell semiconductor nanocrystals, *Small*, 2009, **5**, 154-168.

7 S. Singh, K. C. Barick and D. Bahadur, Fe_3O_4 embedded ZnO nanocomposites for the removal of toxic metal ions, organic dyes and bacterial pathogens, *J. Mater. Chem. A*, 2013, **1**, 3325-3333.

8 W. Yan, H. Fan and C. Yang, Ultra-Fast Synthesis and enhanced photocatalytic properties of alpha-Fe_2O_3/ZnO core-shell structure, *Mater. Lett.*, 2011, **65**, 1595-1597.

9 W. Wu, S. Zhang, X. Xiao, J. Zhou, F. Ren, L. Sun and C. Jiang, Controllable synthesis, magnetic properties, and enhanced photocatalytic activity of spindlelike mesoporous α-Fe_2O_3/ZnO core-shell heterostructures, *ACS Appl. Mater. Interfaces*, 2012, **4**, 3602-3609.

10 A. Kezzim, N. Nasrallah, A. Abdi and M. Trari, Visible light induced hydrogen on the novel hetero-system $CuFe_2O_4/TiO_2$, *Energy Convers. Manage.*, 2011, **52**, 2800-2806.

11 D. Jing, L. Guo, L. Zhao, X. Zhang, H. Liu, M. Li, S. Shen, G. Liu, X. Hu, X. Zhang, K. Zhang, L. Ma and P. Guo, Efficient solar hydrogen production by photocatalytic water splitting: from fundamental study to pilot demonstration, *Int. J. Hydrogen Energy*, 2010, **35**, 7087-7097.

12 V. K. Sharma, R. A. Yngard and Y. Lin, Silver nanoparticles: green synthesis and their antimicrobial activities, *Adv. Colloid. Interface Sci.*, 2009, **145**, 83-96.

13 M. Rai, A. Yadav and A. Gade, Silver nanoparticles as a new generation of antimicrobials, *Biotechnol. Adv.*, 2009, **27**, 76-83.

14 J. S. Kim, E. Kuk, K. N. Yu, J.-H. Kim, S. J. Park, H. J. Lee, S. H. Kim, Y. K. Park, Y. H. Park, C.-Y. Hwang, Y.-K. Kim, Y.-S. Lee, D. H. Jeong and M.-H. Cho, Antimicrobial effects of silver nanoparticles, *Nanomed.Nanotechnol.*, 2007, **3**, 95-101.

15 I. Sondi and B. Salopek-Sondi, Silver nanoparticles as antimicrobial agent: a case study on E. coli as a model for Gram-negative bacteria, *J. Colloid Interface Sci.*, 2004, **275**, 177-182.

16 Y. Zheng, C. Chen, Y. Zhan, X. Lin, Q. Zheng, K. Wei and J. Zhu, Photocatalytic activity of Ag/ZnO heterostructure nanocatalyst: correlation between structure and property, *J. Phys. Chem. C*, 2008, **112**, 10773-10777.

17 R. Georgekutty, M. K. Seery and S. C. Pillai, A highly efficient Ag-ZnO photocatalyst: synthesis, properties, and mechanism, *J. Phys. Chem. C*, 2008, **112**, 13563-13570.

18 A. Kubacka, M. Fernandez-Garcia and G. Colon, Advanced nanoarchitectures for solar photocatalytic applications, *Chem. Rev.*, 2012, **112**, 1555-1614.

19 H. Liu, J. Wu, J. H. Min, X. Zhang and Y. K. Kim, Tunable synthesis and multifunctionalities of Fe_3O_4-ZnO hybrid core-shell nanocrystals, *Mater. Res. Bull.*, 2013, **48**, 551-558.

20 A. A. Shal and A. Jafari, Study of structural and magnetic properties of superparamagnetic Fe_3O_4-ZnO core-shell nanocomposites, *J. Supercond. Nov. Magn.*, 2014, **27**, 1531-1538.

21 C. Karunakaran, P. Vinayagamoorthy and J. Jayabharathi, Non-quenching of charge carriers by Fe_3O_4 core in Fe_3O_4/ZnO nanosheets photocatalyst, *Langmuir*, 2014, **30**, 15031-15039.

22 Z. Xiao, S. Jin, X. Wang, W. Li, J. Wang and C. Liang, Preparation, structure and catalytic properties of magnetically separable Cu-Fe catalysts for glycerol hydrogenolysis, *J. Mater. Chem.*, 2012, **22**, 16598-16605.

23 M. S. Jang, M. K. Ryu, M. H. Yoon, S. H. Lee, H. K. Kim, A. Onodera and S. Kojima, A study on the Raman spectra of Al-doped and Ga-doped ZnO ceramics, *Cur. Appl. Phys.*, 2009, **9**, 651-657.

24 X. Wang, Q. Zhang, Q. Wan, G. Dai, C. Zhou and B. Zou, Controllable ZnO architectures by ethanolamine-assisted hydrothermal reaction for enhanced photocatalytic activity, *J. Phys. Chem. C*, 2011, **115**, 2769-2775.

25 N. Tripathi, K. Vijayarangamuthu and S. Rath, A Raman spectroscopic study of structural evolution of electrochemically deposited ZnO films with deposition time, *Mater. Chem. Phys.*, 2011, **126**, 568-572.

26 Y. Zeng, T. Zhang, W. Fu, Q. Yu, G. Wang, Y. Zhang, Y. Sui, L. Wang, C. Shao, Y. Liu, H. Yang and G. Zou, Fabrication and optical properties of large-scale nutlike ZnO microcrystals via low-temperature hydrothermal route, *J. Phys. Chem. C*, 2009, **113**, 8016-8022.

27 S.-S. Lo and D. Huang, Morphological variation and Raman spectroscopy of ZnO hollow microspheres prepared by a chemical colloidal process, *Langmuir*, 2010, **26**, 6762-6766.

28 J. J. Dong, X. W. Zhang, J. B. You, P. F. Cai, Z. G. Yin, Q. An, X. B. Ma, P. Jin, Z. G. Wang and P. K. Chu, Effects of hydrogen plasma treatment on the electrical and optical properties of ZnO films: identification of hydrogen donors in ZnO, *ACS Appl. Mater. Interfaces*, 2010, **2**, 1780-1784.

29 T. Premkumar, Y. S. Zhou, Y. F. Lu and K. Baskar, Optical and field-emission properties of ZnO nanostructures deposited using high-pressure pulsed laser deposition, *ACS Appl. Mater. Interfaces*, 2010, **2**, 2863-2869

30 G. S. Wu, T. Xie, X. Y. Yuan, Y. Li, L. Yang, Y. H. Xiao and L. D. Zhang, Controlled synthesis of ZnO nanowires or nanotubes via sol-gel template process, *Solid State Comm.*, 2005, **134**, 485-489.

31 P. Laokul, V. Amornkitbamrung, S. Seraphin and S. Maensiri, Characterization and magnetic properties of nanocrystalline $CuFe_2O_4$, $NiFe_2O_4$, $ZnFe_2O_4$ powders prepared by the Aloe vera extract solution, *Curr. Appl. Phys.*, 2011, **11**, 101-108.

32 K. Verma, A. Kumar and D. Varshney, Effect of Zn and Mg doping on structural, dielectric and magnetic properties of tetragonal $CuFe_2O_4$, *Curr. Appl. Phys.*, 2013, **13**, 467-473.

33 Y.-C. Liu and Y.-P. Fu, Magnetic and catalytic properties of copper ferrite nanopowders prepared by a microwave-induced combustion process, *Ceram. Int.*, 2010, **36**, 1597-1601.

34 R. K. Selvan, C. O. Augustin, C. Sanjeeviraja and D. Prabhakaran, Effect of SnO_2 coating on the magnetic properties of nanocrystalline $CuFe_2O_4$, *Solid State Commun.*, 2006, **137**, 512-516.

35 T. G. Altincekic, I. Boz, A. Baykal, S. Kazan, R. Topkaya and M. S. Toprak, Synthesis and characterization of $CuFe_2O_4$ nanorods synthesized by polyol route, *J. Alloys Compds*., 2010, **493**, 493-498.

36 M. M. Rashad, R. M. Mohamed, M. A. Ibrahim, L. F. M. Ismail and E. A. Abdel-Aal, Magnetic and catalytic properties of cubic copper ferrite nanopowders synthesized from secondary resources, *Adv. Powder Technol*., 2012, **23**, 315-323.

37 I. Nedkov, R. E. Vandenberghe, Ts. Marinova, Ph. Thaihades, T. Merodiiska and I. Avramova, Magnetic structure and collective Jahn-Teller distortions in nanostructured particles of $CuFe_2O_4$, *Appl. Surf. Sci*., 2006, **253**, 2589-2596.

38 Y. M. Z. Ahmed, M. M. Hessien, M. M. Rashad and I. A. Ibrahim, Nano-crystalline copper ferrites from secondary iron oxide (mill scale), *J. Magn. Magn. Mater*., 2009, **321**, 181-187.

39 R. Mariappan, V. Ponnusamy and P. Suresh, Effect of doping concentration on the structural and optical properties of pure and tin doped zinc oxide thin films by nebulizer spray pyrolysis (NSP) technique, *Superlattices Microstruct*., 2012, **52**, 500-513.

40 J. Becker, K. R. Raghupathi, St. J. Pierre, D. Zhao and R. T. Koodali, Tuning of the crystallite and particle sizes of ZnO nanocrystalline materials in solvothermal synthesis and their photocatalytic activity for dye degradation, *J. Phys. Chem. C*, 2011, **115**, 13844-13850.

41 L. Jing, Y. Qu, B. Wang, S. Li, B. Jiang, L. Yang, W. Fu, H. Fu and J. Sun, Review of photoluminescence performance of nano-sized semiconductor materials and its relationships with photocatalytic activity, *Sol. Energy Mater. Sol. Cells*, 2006, **90**, 1773-1787.

42 S. W. Jung, W. I. Park, H. D. Cheong, G.-C. Yi and H. M. Jang, Time-resolved and time-integrated photoluminescence in ZnO epilayers grown on Al_2O_3 (0001) by metalorganic vapor phase epitaxy, *Appl. Phys. Lett*., 2002, **80**, 1924-1926.

43 J. Schneider, M. Matsuoka, M. Takeuchi, J. Zhang, Y. Horiuchi, M. Anpo, D. W. Bahnemann, Understanding TiO_2 photocatalysis: mechanisms and materials, *Chem. Rev*., 2014, 114, 9919-9986.

44 A. Layek, B. Manna and A. Chowdhury, Carrier recombination dynamics through defect states of ZnO nanocrystals: from nanoparticles to nanorods, *Chem. Phys. Lett*., 2012, **539-540**, 133-138.

45 C. Karunakaran, P. Anilkumar and P. Gomathisankar, Kinetics of Ag/TiO_2-photocatalyzed iodide ion oxidation, *Monatsh. Chem*., 2010, **141**, 529-537.

46 C. Karunakaran, P. Gomathisankar and G. Manikandan, Preparation and characterization of antimicrobial Ce-doped ZnO nanoparticles for photocatalytic detoxification of cyanide, *Mater. Chem. Phys*., 2010, **123**, 585-594.

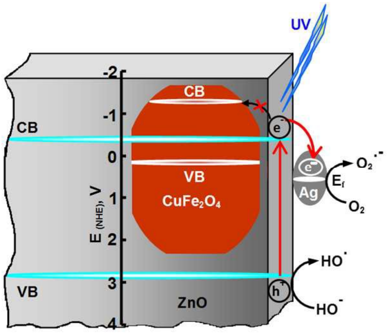

Charge carrier-non-quencing magnetic core implanted in nanocrystalline ZnO and deposited with metallic Ag for superior bactericidal and photocatalytic activities